Optics and Lasers in Engineering 184 (2025) 108631

Contents lists available at ScienceDirect

Optics and Lasers in Engineering

journal homepage: www.elsevier.com/locate/optlaseng

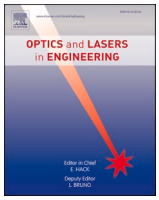

High-speed low-cost line-field spectral-domain optical coherence tomography for industrial applications

Xingyu Yang [a,b], Zijian Zhang [a,b], Xinhua Li [c], Hungyen Lin [d], Samuel Lawman [a,b], Stoyan Stoyanov [e], Timothy Tilford [e], Yihua Hu [f], Yaochun Shen [a,*], Yalin Zheng [b,g,h]

[a] Department of Electrical Engineering and Electronics, University of Liverpool, Liverpool L69 3GJ, UK
[b] Department of Eye and Vision Sciences, University of Liverpool, Liverpool L7 8TX, UK
[c] Department of Automation, Tsinghua University, Beijing 100084, China
[d] School of Engineering, Lancaster University, Lancaster LA1 4YW, UK
[e] School of Computing and Mathematical Sciences, University of Greenwich, London SE10 9LS, UK
[f] Department of Engineering, King's College London, London WC2R 2LS, UK
[g] Liverpool Centre for Cardiovascular Science, University of Liverpool and Liverpool Heart & Chest Hospital, Liverpool L7 8TX, UK
[h] St Paul's Eye Unit, Liverpool University Hospitals NHS Foundation Trust, Liverpool L7 8XP, UK

ARTICLE INFO

Keywords:
Optical coherence tomography
Low-cost
Non-destructive evaluation
3D imaging
High-speed
Simulation

ABSTRACT

The applications of Optical Coherence Tomography (OCT) systems have been extensively explored in clinical settings and have attracted growing interest in other fields. Factors such as speed and cost are often prioritized over high resolution and power efficiency in industrial applications. Modern OCT systems typically operate at speeds between 20k-70k A-scans/s and are priced at least $50k. We report a line-field OCT with a high imaging speed of 430k A-scans/s, by operating a 2D camera in 8-bit mode, at a cost of $3.2k. The reported OCT system provides an axial resolution of 9 μm in air and achieves a maximum on-axis signal-to-noise ratio and sensitivity of 68.8 dB and 88.8 dB, respectively. We demonstrate the practical use of the system by measuring, visualizing, and segmenting samples of Printed Circuit Boards, pharmaceutical tablets, and pea seeds.

1. Introduction

OCT is a non-invasive, cross-sectional imaging modality based on interference between the sample and reference signal for optical ranging in the axial direction [1–4]. Scanning-point (SP) based Fourier Domain (FD) configurations, including Spectral Domain (SD) [5] and Swept Source (SS) [6] OCT, have been well-developed and implemented commercially in medical imaging, especially in ophthalmology [3,7]. FD-OCT configurations benefit from an intrinsically higher signal-to-noise ratio (SNR) and speed than the predecessor Time-Domain (TD) OCT systems [8]. The point-by-point (raster) scanning pattern is commonly employed in SP-OCT systems. The probe beam is generally steered by a two-dimensional (2D) scanning system and A-scans are captured sequentially to achieve volumetric imaging. The cost of commercially available SP-OCT systems remains high ($50k – $250k), limiting the wider application of the technology. Various efforts have been made to balance trade-offs such as size, SNR, speed, and cost of SP-OCT systems [9–12]. Particularly, the speed of the point-scanning-based systems is mainly limited by the sensor (linear detector arrays), the light source for *in-vivo* illumination, and the scanning system. Typical commercially available SD-OCT machines operate at speeds between 20k-70k A-scan/s, as summarized in [13]. SS-OCT systems break the speed bottleneck by using wavelength-tuning laser and a balanced detection configuration to acquire OCT data at the cost of a higher price [6]. The combination of cost-effectiveness and speed is a logical development within current research paradigms.

Line-field Spectral-domain OCT (denoted as LF-OCT for simplicity) is an OCT variant with growing interest that illuminates the sample with a line-shaped beam and detects parallelly [14]. The sensor in this configuration is replaced by 2D area cameras instead of 1D line cameras in the scanning-point systems. Consequently, LF-OCT can capture an entire B-scan image in a single-shot fashion, necessitating only a single-dimensional scanning mechanism for 3D imaging. This configuration can achieve a reduced acquisition time compared to the point-by-point acquisition and scanning mode [15,16]. Another advantage of line illumination is that the optical power is distributed

* Corresponding author.
E-mail address: y.c.shen@liverpool.ac.uk (Y. Shen).

https://doi.org/10.1016/j.optlaseng.2024.108631
Received 17 June 2024; Received in revised form 23 September 2024; Accepted 2 October 2024
Available online 9 October 2024

along the line instead of a single point, enabling a higher imaging speed and a lower risk of damage. These advantages allow LF-OCT systems to overcome the trade-offs and use low-cost components while maintaining high performance. The majority of the current investigations of LF-OCT systems focus on achieving high performance, including ultra-high axial resolution (e.g. <3 μm) [15], lateral resolution [17], and ultra-high speed (e.g. A-scan rate at MHz) [18]. Limited research on variants of low-cost LF-OCT can be found in [19–21] and they are summarized in our previous publication [16].

Another parallel detection paradigm is Time-Domain Full-Field OCT (denoted as FF-OCT for simplicity. In contrast to the conventional TD-OCT, FF-OCT systems perform plane detection based on full-field illumination. While FF-OCT may offer certain advantages in terms of lateral resolution and image quality for surface layers, it generally has slower 3D acquisition times compared to the rapid image capture of SD-OCT. In addition, FF-OCT configuration requires either a phase-shifting mechanism (Piezo-electric ceramic or wave plates) [22] or high-precision motorised stages [23].

The acquisition speed and cost of OCT systems are prioritized in broader industrial adoption [24–30]. Conventionally, a bit-depth of 12 or higher is utilized for the digitizers or sensors in OCT systems to preserve the inherent dynamic range when imaging through scattering tissue [31]. However, the data transfer rate (as high as 38 GB/s) of high bit-depth high-speed systems can be demanding and requires high-spec computer hardware to handle. The size of the total data volume can exceed 100 GB per patient in a clinical setting [32]. The slow speed for storing, processing, and visualizing such large data hinders the acute flow in clinics, reducing the practicality of OCT, especially for OCT Angiography data that records data at multiple time points [33]. Early studies demonstrated a low system SNR of 46 dB [34] and 37 dB [35] using 8-bit digitizers. Later studies provided noise analysis and proved the feasibility of using 8-bit Analogue-to-Digital Conversion (ADC) with little sensitivity reduction (~1 dB) compared to 12 bits and above [32, 36]. Although lower bit-depth inhibits the OCT inherent dynamic range, a deep learning-based method has been proposed to reconstruct high SNR signals [37].

In this paper, we report the development of a novel variant of a low-cost LF-OCT system that uses a 2D camera retailed at $450 (price retrieved on May 2024) to reach a B-scan rate of 690 Hz or an A-scan rate of 430k Hz at 8 bits. The total cost of the system is around $3200. Compared to using the 12-bit mode of the USB3 Vision camera, the 8-bit mode increases the acquisition speed by about 60 %, data size reduction by 50 % and 0.7 dB sensitivity loss under the same experimental condition. The system can achieve an image depth range of 2.7 mm with an axial resolution of 9.0 μm in air. We demonstrate the simplicity of the system design, performance quantification, and the justification of using 8-bit ADC. We also present the imaging, 3D visualization, and quantification of three industrial Non-Destructive Evaluation (NDE) applications using the developed system.

2. System setup

2.1. Optical configuration

Fig. 1. shows the optical schematic of the developed LF-OCT system. The light source of the system is a superluminescent diode (SLD) (EXS210040–01, Exalos) with a center wavelength of 838 nm and a full width at half maximum (FWHM) bandwidth of 49 nm. The SLD is controlled by a constant current driver. A two-times beam expander is used to increase the beam diameter, resulting in increased line pairs that are illuminated on the diffractive grating. A cylindrical lens (CYL) is used to generate the line illumination. As illustrated in Fig. 1(b), in the vertical optical view, the cylindrical lens focuses the illumination of the sample into a line. The length of the line is determined by the collimated beam diameter, which is 11 mm at $1/e^2$ of the maximum intensity in this design. The constant e denotes Euler's number. A 50:50 non-polarizing beam splitter is employed to form the free-space Michelson interferometer.

In the imaging path, the light scattered from the illuminated area of the sample is collected by using an achromatic lens L1 and then imaged through a camera lens L2 onto the 2D Complementary Metal-Oxide Semiconductor camera plane. Together with a Volume Phase Holographic transmission grating, the 2D spectrometer of the system is formed. The diffraction angle of the grating is optimized to maximize the diffraction efficiency. The 2D camera has 816 × 624 pixels and the size of each pixel is 9 × 9 μm^2. The 2D camera allows 8-bit ADC with a corresponding read-out rate of 690 fps. The read-out rate is bottlenecked by the USB 3.1 data transmission interface. The sample is imaged onto the camera plane by the imaging optics with a magnification of 0.5. The lateral scanning is achieved by using a high-speed motorized stage. The overall dimension for the system is about 20 × 15 × 20 cm^3.

The spectrograph calibration is achieved by placing a slit vertically at the center of the focal plane of the sample arm. A mercury-argon light source (USB-Hg-NeAr, Princeton Instrument) is placed behind the slit to provide a known wavelength. The calibration light source is placed behind a slit that is placed at the central position of the beam path at the focal plane of the sample arm. Four points with known wavelengths were recorded and a second-order polynomial fitting was applied for calibration. To demonstrate the system performance, a MATLAB-based driver program is developed in-house to control the B-scan live

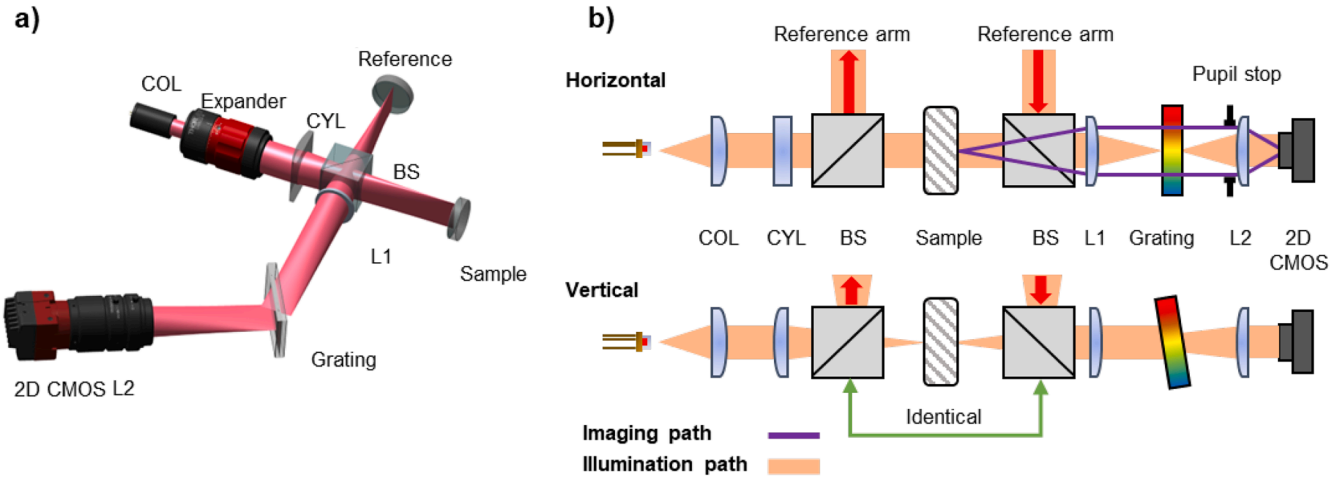

Fig. 1. (a) The design of the developed LF-OCT system. COL: aspheric collimation lens; CYL: cylindrical lens; BS: beamsplitter; L1–2: achromatic doublet lenses. (b) The horizontal and vertical perspective of the design. The BSs on both sides of the sample are identical.

display, synchronization, 3D image acquisition, and data visualization. A flowchart and description of the software are detailed in the Supplementary Material.

2.2. Design considerations

To optimize system performance for industrial needs, speed, cost, and imaging depth were prioritized over factors such as resolution and power efficiency. The camera sensor has a pixel pitch of 0.065 nm in the spectral domain, allowing a theoretical axial measurement range of 2.7 mm. The sensor captures a spectral bandwidth of 53.4 nm, which represents approximately 63 % of the spectral range ($1/e^2$) of the light source. This configuration reserves the central portion of the spectrum and 87 % of the light power. The spectrum is shown in Fig. 3. a). As the foot of the spectrum is cut off, the measured axial resolution of the system is 9.0 μm, rather than the reported 8.3 μm in our previous work [16]. Assuming 8-bit ADC and near camera saturation, the signal is represented with 8-bit resolution at the spectral peak. At the point where the intensity falls to $1/e^2$ of its peak value, the resolution degrades to only 5 bits. The designed spectral bandwidth coverage of the system is around the FWHM value of the SLD. The intensity of the spectrum will be halved at both edges of the spectrum and all spectral points are measured by a relatively high bit resolution of 7 or more. We traded off the axial resolution and power efficiency with a higher bit resolution for the foot of the spectrum, which is particularly beneficial for detecting OCT interference.

Moreover, the collected spectrum is effectively truncated by the finite width of the detector, leading to increased sidelobes in A/B-scan signals after the Fast Fourier Transform. As discussed in [29], a Tukey window is applied for spectrum shaping. It has a negligible effect on axial resolution but significantly reduces the sidelobes. In principle, SLDs with a narrower bandwidth can be used to improve the light power efficiency and avoid sidelobes. However, this will lead to a reduced spectral dynamic range of the system, particularly at both ends of the spectrum where the signal is lower.

2.3. Simulation

The imaging path of the developed system has been simulated and evaluated using ZeMax, as shown in Fig. 2. a). Note that the model of the camera lens L2 is not included in the ZeMax lens catalogue, a paraxially approximated perfect lens with the same focal length is modelled for best-case scenario simulation instead. Fig. 2(b). shows the Root-Mean-Square (RMS) spot radius on the camera sensor plane at different wavelengths and lateral locations. The simulation is optimized for the most balanced on- and off-axis performance. At the center wavelength $\lambda_0 = 840$ nm, the on-axis, 2.75 mm off-axis, and 5.50 mm off-axis RMS spot radii are 5.7 μm, 5.9 μm, and 13.2 μm, respectively. However, for non-central wavelength $\lambda = 865$ nm, while the on-axis spot radius is 8.0 μm, the spot radius at the edge of the line FOV degrades to 16.3 μm. The increased spot diameter at the camera sensor is expected to lead to lower sensitivity at the edges of the line illumination.

3. System characterization

3.1. System performance

The system performance is characterized by experimental measurements. Fig. 3(a) shows the spectrum of the SLD measured by a commercial spectrometer (USB2000+, OceanOptics). Fig. 3(b) shows the spectrum and interference pattern at Optical Path Difference (OPD) = 0.25 mm using the developed LF-OCT system.

Theoretically, the axial resolution is the FWHM of the envelope of the depth point spread function of the light source. The theoretical axial resolution in the developed system is 8.5 μm in air due to the camera sensor width. Experimentally, the axial resolution is measured by taking an A-scan signal obtained close to the zero OPD and applying a Gaussian fit on the finite data points. The measured axial resolution is 9.0 μm, which is in high agreement with the theoretical value. The discrepancy of 0.5 μm is likely caused by intrinsic optical aberrations, as shown in Fig. 3(c). Zero-padding together with linear interpolation with a factor of 2 was used to resample the interference data to avoid interpolation error at the frequency oscillation period approaches as small as two pixels in the spectrometer [38,39].

The sensitivity roll-off of the system is characterized by acquiring the A-scan signals for the on-axis point at varying axial positions of a mirror sample, as shown in Fig. 3(d). The two dashed lines indicate the theoretical roll-off curves at spectral resolution equivalent to 1 (0.065 nm)

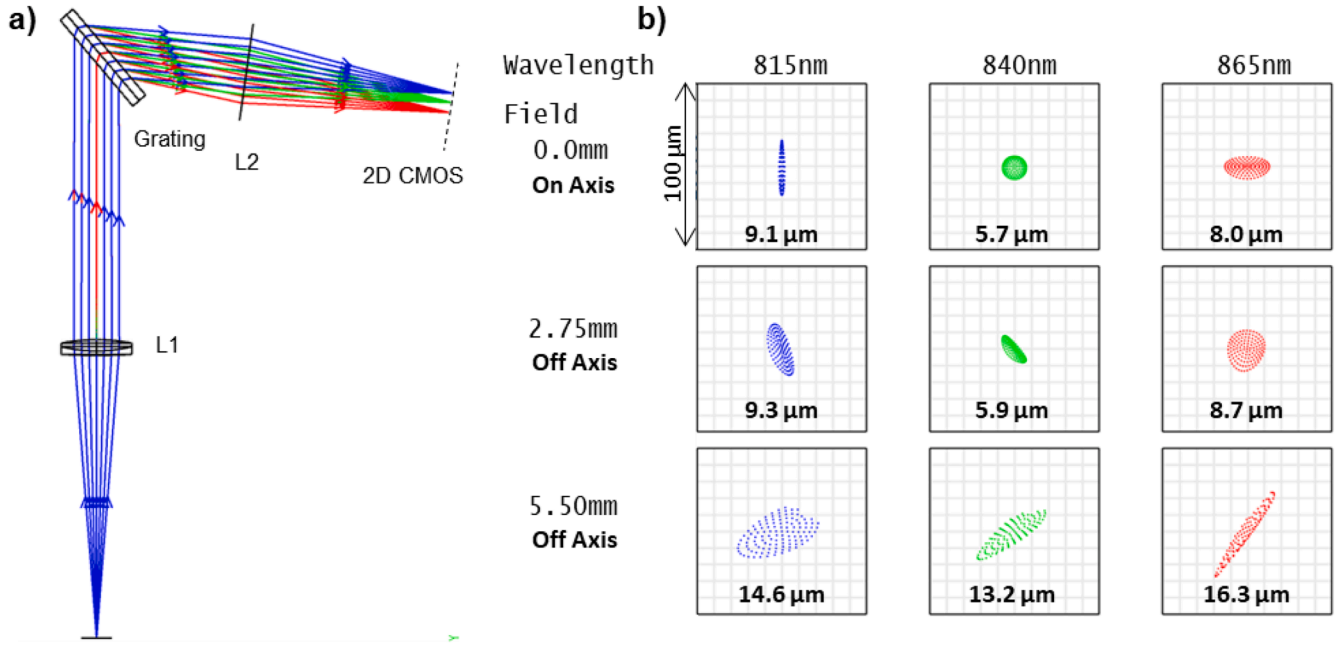

Fig. 2. (a) ZeMax simulated imaging path of the developed LF-OCT system. (b) Simulated spot diagrams at three field positions corresponding to three wavelengths. The RMS diameters of the spots are marked individually.

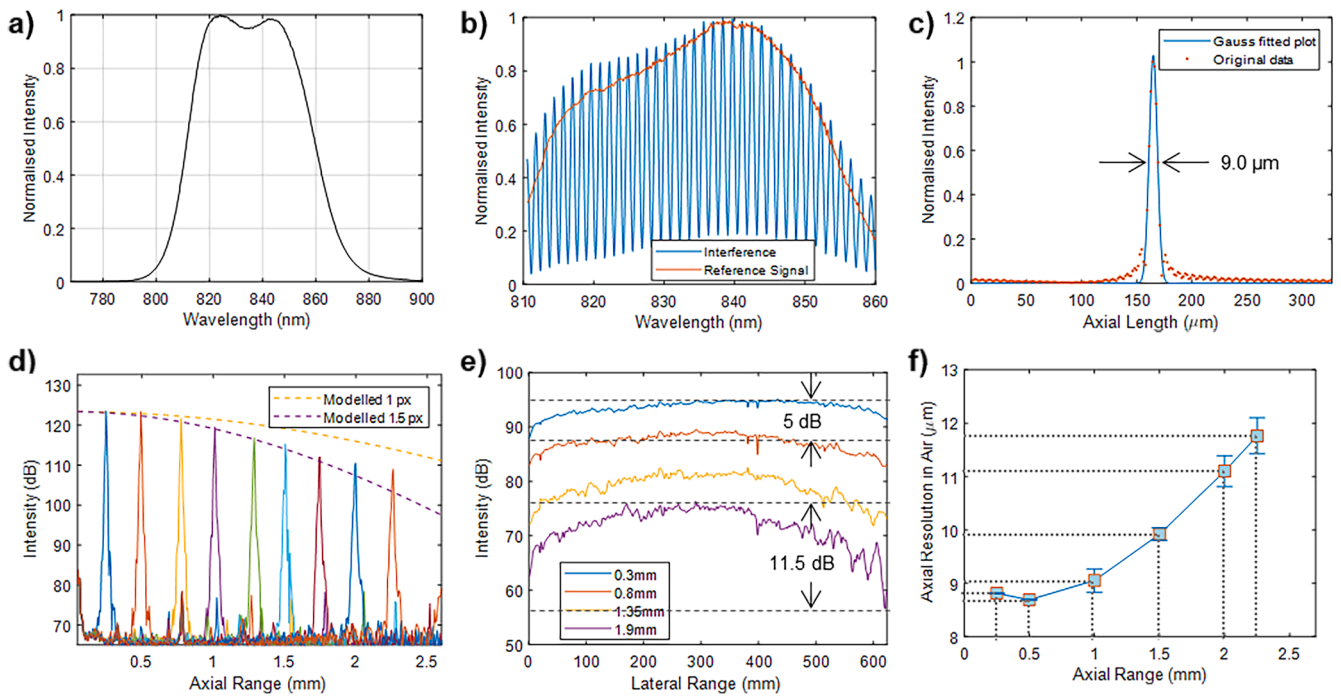

Fig. 3. (a) The spectrum of the SLD measured by a commercial spectrometer. (b) The spectrum and interference pattern measured by the developed LF-OCT system. (c) A Gaussian fit of the zero-padded A-scan that shows an axial resolution of 9.0 μm in air. d) Measured A-scan signals at varying axial positions of a mirror sample. Two dashed lines indicate the respective roll-off curves at two spectral resolutions. (e) Measured signals across the B-scan image at different axial positions of a mirror sample. The black dashed lines show the intensity difference between the center and the edge of the line. (f) the axial resolutions measured at all depths.

and 1.5 (0.975 nm) pixels. The inhomogeneous line illumination on the sample affects the SNR in the lateral positions. The A-scan signals at different lateral positions are measured from the mirror sample to characterize the position-dependent SNR, as shown in Fig. 3(e). At the axial position of 0.3 mm, the SNR deficit between the edge and the center of the line is around 5 dB. The deficit is increased to 11.5 dB at the axial position of 1.9 mm. This degradation is due to the off-axis performance of the imaging optics and has been reported in [17,40]. The experimentally measured total axial range was 2.7 mm which agrees well with the theoretical value. The axial resolution at all depths was measured and its roll-off is shown in Fig. 3(f). The roll-off is caused by the nonuniform spectral resolution of the system [17].

As shown in Fig. 4(a), the lateral resolution of the developed system is determined by imaging a resolution test target (USAF 1951 chromium positive, Thorlabs) and identifying the smallest resolvable element. The step resolution of the motorized stage was set to 20 μm for acquisition. Fig. 4(b) shows the enlarged view of the central part of the target, while (c) and (d) are the intensity profiles across the line pairs that demonstrate the minimally resolvable pattern. As a result, the lateral resolution along the line direction is group 4 element 6, or 35.1 μm; along the scan direction is group 4 element 5, or 39.4 μm. Note that the system is limited by the step resolution in the scan direction rather than optical resolution. The choice of 20 μm is a balance of matching the lateral resolution in both directions and system speed.

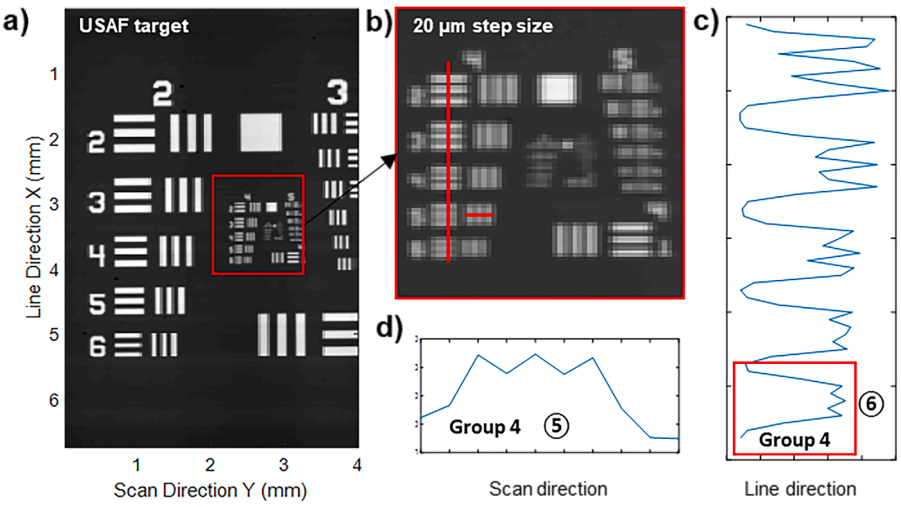

Fig. 4. (a) The *en-face* OCT image of a USAF resolution test target. (b) the zoom-in view at the center of the target, measured with a step resolution of 20 μm. (c) and (e) are the intensity profiles across the line pairs.

3.2. Signal-to-noise ratio (SNR)

Several groups have analyzed the SNR in OCT and have shown the sensitivity advantage of Fourier domain techniques over time-domain OCT [41]. We follow the analysis of [32] and recognize three noise sources that dominate SD-OCT: thermal/electrical, relative intensity noise (RIN), and shot noise. The thermal/electrical noise is introduced by the detector and, in general, is not signal-dependent. The low-cost but thermally unregulated SLD used in the developed system suffers from temperature drifts, causing RIN [16,42]. Shot noise arises from the statistical nature of photons. Different from this [32], we numerically modelled the random occurrence of photon absorption events in a photodetector following the Poisson process. The RIN and thermal/-electronics noise are not considered in this model because they are comparatively small [41]. Another source of quasi-noise in the developed system is quantization error, which is induced through distortions caused by the finite bit-depth of the camera ADC circuit. Upon digitization, the analogue signal is converted to a digital signal with a finite bit depth. The detector used in the system has a pixel electron well depth of 94,000 e^- on 12-bit mode. The impact shot noise and quantization noise on SNR can be modelled at 6-, 8-, 10-, and 12-bit depths. The modelled theoretical SNR values were compared against experimental values measured following a typical setup [43] as shown in Fig. 5(a).

The setup comprised two silver mirrors placed normal to the OCT beam, at the focal planes of the reference and sample arms. Both arms were attenuated by the same Neutral Density (ND) filter with an Optical Density (OD) = 1.0 inserted between the mirrors and the focusing lens. The camera reached near saturation with the exposure time set to 500 μs as the default measurement configuration. The SNR, or dynamic range of the OCT system can be measured by finding the A-scan peak signal of the mirror and the standard deviation of the noise floor, as shown in Fig. 5 (b) and (c). The noise floor is measured by repeating the measurement without the mirror at the sample arm. As the intensity is proportional to the photocurrent collected by the sensor, the SNR in the logarithm scale can be calculated as:

$$SNR(dB) = 10log\left(\frac{{i_{signal}}^2}{{\sigma_{noise\ floor}}^2}\right)$$

As shown in Fig. 5(d), the solid blue line represents the theoretical shot-noise limited SNR at different bit depths, while the dashed red line indicates SNR with quantization. The shot-noise limited SNR is bit-depth independent, hence little variation is seen from the plot. Experimentally, The SNR values of the 8-, 10-, and 12-bit depths were measured with a mirror sample placed 0.25 mm away from zero OPD. The measurement is repeated 5 times with the median values and standard deviation (std) calculated. The 6-bit depth values are converted by rescaling the measured 8-bit results. The median values corresponding to 6-, 8-, 10, and 12-bit modes are 64.74 dB, 66.81 dB, 67.18 dB, and 67.29 dB, respectively. The std values are 0.18, 0.19, 0.23, and 0.24, respectively. The discrepancy between the experimental and theoretical values could stem from the unmodelled electronic noise and RIN [16]. Notably, with the same camera exposure time and external light power, we observed a nearly 4 times well depth decrease when switching from 10- or 12-bit ADC modes to 8-bit. This is a known phenomenon confirmed by the camera manufacturer. The exposure time was set to accommodate the lower effective well depth at 8-bit mode. This is reflected in the numerical model assuming 25 % of well depth usage.

The result indicates the impact of bit-depth on the SNR values of a shot-noise-limited OCT system. The loss at 8 bits and 6 bits are ~0.7 dB and 5.0 dB, respectively. The experiment SNR values start to converge to the theoretical values as the bit rate decreases showing the system is bit-depth limited instead of shot-noise limited. Notably, by increasing the exposure time and fully utilizing the well depth, the measured SNR is 72.8 dB, which is 4 dB higher than the 8-bit mode. Nevertheless, as the system was configured to operate at 25 % of the well depth, this SNR difference does not directly reflect the impact of quantization error.

Moreover, Fig. 6(a) shows the single-frame B-scan images of a scotch tape sample, acquired by both 8- and 12-bit modes of the camera in the developed LF-OCT system with integration time set to 100 μs. The acquired B-scan images consist of 624 A-scans, equivalent to 11.2 mm laterally. Fig. 6(b) shows the averaged plot of the central 10 A-scans of the two B-scan images after subtraction of background images. The 2D images demonstrate a visually indifferentiable SNR difference, while the 1D results show a <1 dB difference in SNR values obtained from the two modes. The calculated Pearson correlation coefficient of these two signals is 0.948, exhibiting a high degree of agreement.

3.3. Sensitivity

The sensitivity of the system was calculated by following the measurement procedures described in [43]. Since the reference arm is attenuated with an ND filter, the sensitivity of the OCT system can be

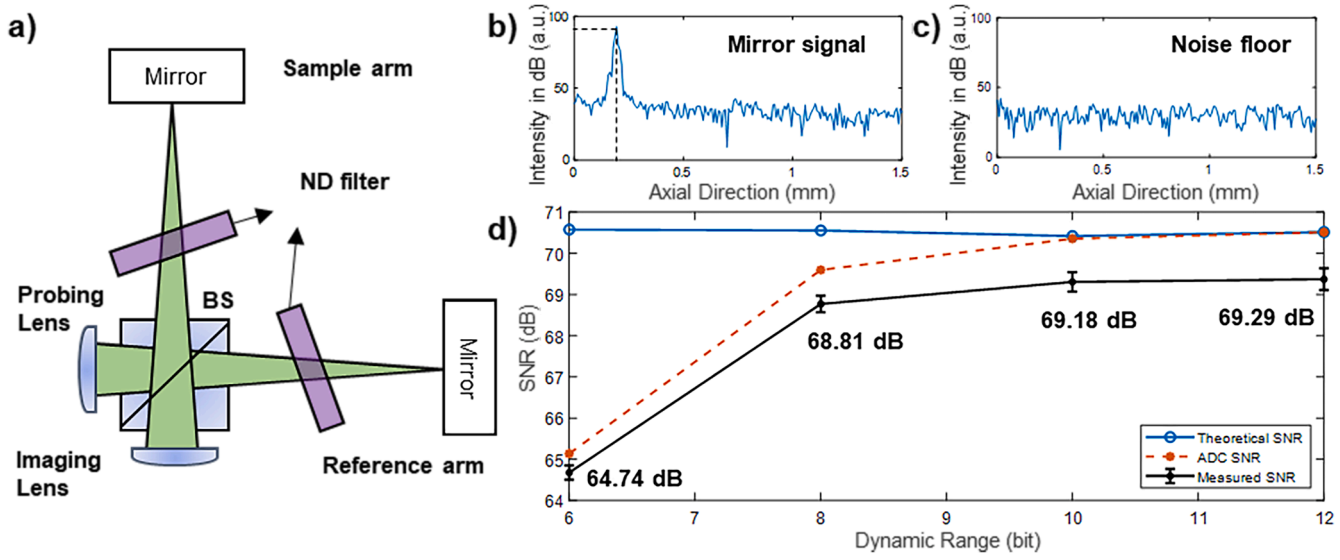

Fig. 5. (a) The schematic for OCT sensitivity measurement setup. (b) The A-scan signal from a mirror sample. (c) The A-scan signal with no presence of a sample. (d) The measured SNR at different bit depths compared against the theoretical shot-noise-limited SNR and numerically modelled SNR with analogue-to-digital conversion.

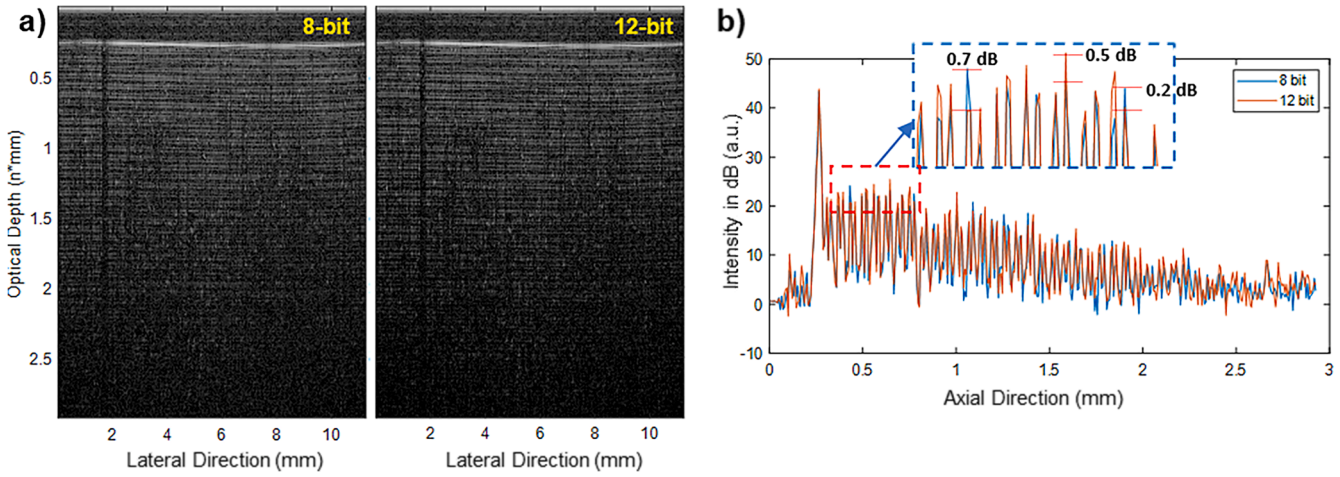

Fig. 6. (a) The B-scans of a scotch tape measured using 8- and 12-bit depth. (b) the 10 averaged A-scans at the center of the B-scans and its zoom-in view for comparison.

calculated following:

$$Sensitivity(dB) = 10\log\left(\frac{{i_{signal}}^2}{{\sigma_{noise\ floor}}^2}\right) + 10\log\left(T^2\right)$$

Where T denotes the transmission of the filter, $T = 10^{-OD}$. The power of 2 is due to the light double-passing through the filter. The sensitivity of the developed system is 88.8 ± 0.2 dB with the OD = 1.0 filter applied. The power of the probe beam is about 2.8 mW.

3.4. Data processing

We aim to quantitatively measure the layers of the samples by extracting them from the background using segmentation, which is an important technique in image analysis aiming to capture the edges of the objects. The segmentation method we propose is a modification of the method reported in [16,44]. The method encompasses three main steps in processing: (1) edge-preserving image smoothing with a non-local means filter; (2) gradient-based peak finding; (3) search region definition and peaks finding.

3.4.1. Pre-processing

As the B-scan images of the developed LF-OCT system are captured in a single-shot fashion, the cross-correlation alignment and histogram equalization of signal intensity of adjacent A-scans as reported in [45] are not needed. Instead, these preprocessing steps are performed on neighboring B-scans of the data acquired by our developed system. Each B-scan image was denoised using an edge-preserving non-local means filter [46] and followed by an optional median filter with a 3 × 3 kernel to highlight the interfaces.

3.4.2. Gradient-based peak finding

As only the vertical interfaces were to be segmented, we employed the conventional directional gradient algorithm with a Sobel operator. The peaks of each A-scan signal correspond to the interfaces in the B-scan images. The gradient peaks can be found by applying a simple peak detector.

3.4.3. Search region

The search region is defined by setting a number of parameters: (1) the starting A-scan location with meaningful signal in the B-scan and searches towards both ends; (2) tolerance for isolated noise pixels or signal gaps. and replacing the outliers with the same axial location as the previous point; (3) peak number, prominence and distance, which are sample-specific.

4. Applications

We present three applications of the developed high-speed LF-OCT system to non-destructively evaluate polymer-based coatings used in electronics, pharmaceutics and plants.

4.1. Printed circuit boards (PCBs)

Conformal coating is a transparent layer that protects PCBs from harsh environments [47]. The thickness and integrity of the coating are of high importance in its effectiveness. The conventional inspection method is the metallographic section, which requires cutting the PCB and examining the cross-sectional view under a microscope [48]. The possibility of examining the coating thickness non-destructively with OCT has been reported in [16,30,49,50]. We present the visualization and measurement of the coating and the surface-mounted components of a PCB sample with the highest speed and lowest cost with the developed OCT system. The sample imaged an off-the-shelf PCB provided by Sci-jet (Model: SJ-IO-RB24 Monitor). Fig. 7(a) shows the photograph of the imaged area of 10 × 10 mm^2, consisting of four resistors, the base, and copper traces.

The same area is scanned and visualized in Fig. 7(b), resulting in a total volume size of 10 × 10 × 2.7 mm^3. The total data points are 600 (lateral) × 500 (scan) × 816 (axial, zero-paddded), equivalent to 500 B-scans. With the 690 Hz B-scan rate of our system, acquiring the entire data volume takes only <1 second with the developed system, leading to a volumetric scanning speed of 10 × 10 × 2.7 mm^3/s. Fig. 7(c) illustrates the interpretation of B-scan images of the PCB sample. The orange line and green lines show the segmented results of the coating layer and base layer of the PCB. The A-scan profiles of the yellow dashed lines are shown in the figure underneath, clearly showing the signal peaks of coating, the base, and auto-correlation artefacts. The measured thickness from B-scans is 106.3 ± 16.0 μm and is consistent with the results in [16].

The *en-face* images at four axial locations of the sample are shown in Fig. 7(d). The first air-coating interface is located at the Depth = 0.3 mm location; the surfaces of the resistors are located at the Depth = 0.35 mm; the second air-coating interface is the PCB base coating, which is situated at Depth = 0.63 mm; the surface of the PCB base and copper traces are located at Depth = 0.8 mm.

4.2. Pharmaceutical tablet film coating

The process of coating tablets with one or more layers of polymer is ubiquitous in pharmaceutical manufacturing to enhance visual

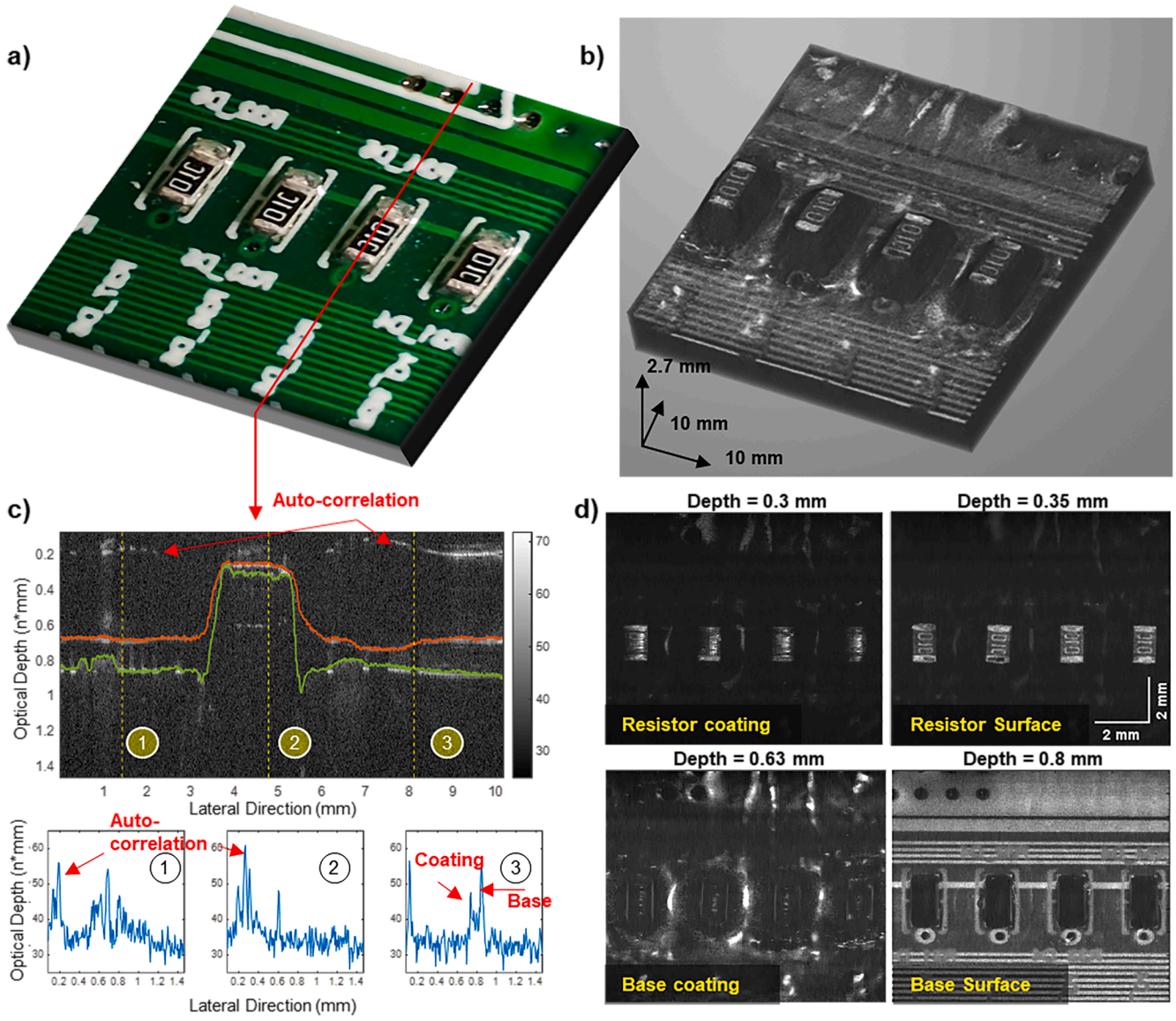

Fig. 7. Measurement of Printed Circuit Board sample using the low-cost LF-OCT system. (a) The photograph of the sample. (b) The volume visualization of the 3D OCT measurement. (c) the B-scan image of the sample, with the coating and base layers indicated by the orange and green solid lines. The corresponding A-scan signals of the yellow dashed lines are shown below. (d) the *en-face* OCT images of the four featured locations of the sample.

attractiveness, taste masking, and more importantly, for engineering drug release profiles. Amongst many techniques such as terahertz pulsed imaging, near-infrared, and Raman spectroscopy, OCT is an emerging non-destructive modality that can resolve coating layers as thin as 20 μm for both off-line and in-line operations [28,51–54]. To enable greater OCT adoption, here we apply our developed system on a pharmaceutical tablet coated using a bespoke laboratory coating unit developed in [53]. In particular, Fig. 8(a) shows the front and back of the tablet where a total area of 8 × 8 mm^2 was scanned on both surfaces. The corresponding 3D visualization of the front surface is shown in Fig. 8(b). B-scans of the red dashed lines in Fig. 8(a) are shown in (c) and (d), where air-coating and coating-core interfaces are segmented and highlighted by the red and yellow solid lines. Note that the B-scan images presented here are smoothed and filtered following the aforementioned data processing steps. Using the previously reported refractive index n = 1.61 [53], the thickness profile is presented in Fig. 8(e) while the distribution histogram is shown in f). The average thickness is 235.3 ± 9.3 μm and is in close agreement with [53]. Without a loss of accuracy, this thickness value is also consistent with the value produced when the camera operated in 12-bit mode.

4.3. Pea seed

Monitoring the inner structure of pea seeds during different germination stages enables the assessment of their maturity, developmental status, and nutrient reserves, thereby determining the quality and growth potential [55]. Previously, SP-OCT systems have been used to characterize the internal structure of seeds [27,29,56,57]. We present, to the best of our knowledge, the first measurement of pea seeds with the LF-OCT system using our configuration. The developed system contributes to further reducing detection costs and expanding application scenarios.

To corroborate the OCT images of the seeds, complementary microscopic images were captured from sections of the seeds. Initially, the cross-sectional images of the seed samples were acquired using OCT, followed by sectioning the measured seed samples for microscopic examination, as shown in Fig. 9(a). For experimentation, three different perspectives of pea seed (Carouby de Maussanne) were selected to ascertain the optimal locations for observing, as shown in Fig. 9(c). Initially, OCT cross-section images were captured at specific regions (2.7 mm in depth and 3 mm in lateral) including the plumule, hilum, and

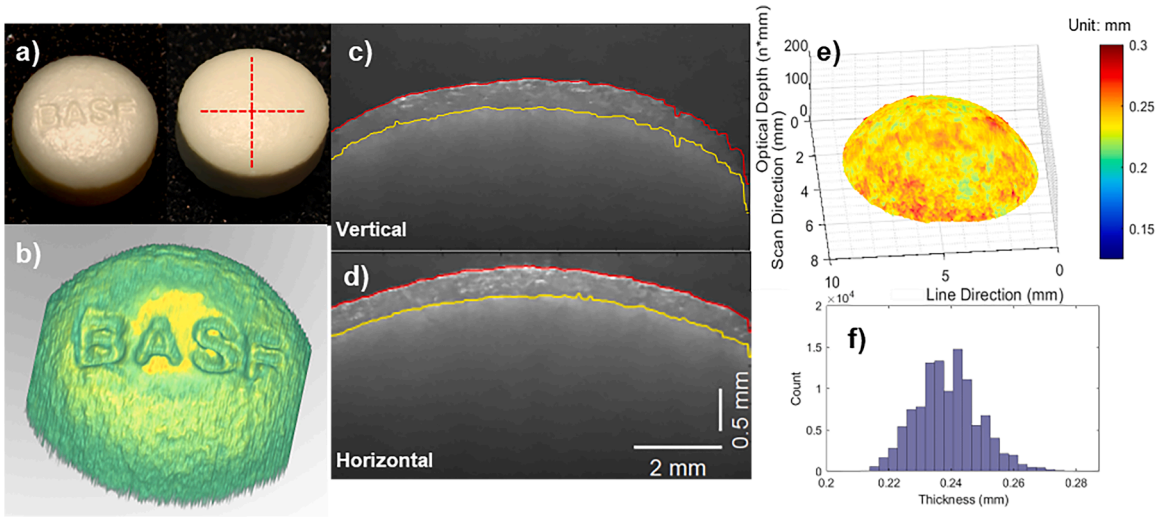

Fig. 8. Measurements of a coated tablet sample using the low-cost LF-OCT system. (a) shows the photographs of the front and the back of the tablet. (b) The visualisation of the 3D OCT measurement of the front with the embossing. (c) and (d) are the pre-processed B-scan images corresponding to the vertical and horizontal red dashed lines in (a). The red and yellow solid lines indicate the segmented layers of the sample. (e) The thickness map of the sample in 3D axis. (f) The coating thickness distribution of the tablet.

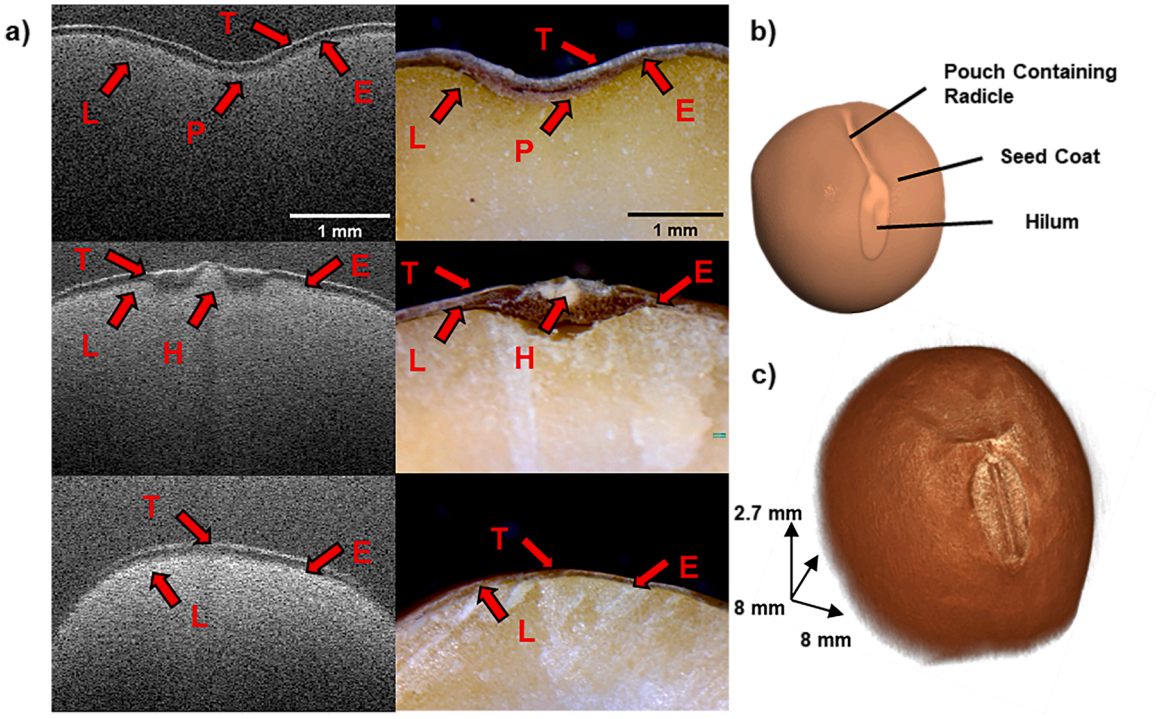

Fig. 9. Measurement of a *Carouby de Maussanne* seed sample using the low-cost LF-OCT system. (a) the comparison of OCT B-scan images between the sectioned microscopic images at the same locations of the pea seed. T: Testa; P: Pouch; containing; L: cotyledon; H: Hilum; E: Endocarp. (b) The exterior structure illustration of the seed. (c) The visualization of the 3D OCT measurement.

seed coat. Subsequently, the samples were sectioned at the exact locations imaged by OCT: the first sample at the plumule, the second at the hilum, and the third at the seed coat. Fig. 9(d) shows the reconstructed 3D OCT data visualisation of pea seeds at the size of $8 \times 8 \times 2.7$ mm^3, captured in about 0.7 s.

The results demonstrate that the developed LF-OCT system is capable of accurately imaging and quantitatively measuring the surface and inner structure of PCBs, tablets, and seeds. The acquisition speed is about 17 times faster than the 40k A-scans/s SP-OCT counterpart. The system has the potential to be expanded in industrial NDE for post-inspection and in-line monitoring for quality assurance.

5. Discussion and conclusions

In conclusion, we report the development and evaluation of a low-cost, high-speed LF-OCT system suitable for several industrial applications. The system can be constructed with off-the-shelf components for a total of $3.2k that reaches a speed of 690 B-scans/s or 430k A-scans/s. The cost is significantly lower than, to the best of our knowledge, any reported OCT systems using scientific-grade cameras [9,16].

The practical performance of the system is evaluated and compared against the theoretical expectations. The design presents several trade-offs that can be refined. First, the slit aperture for crosstalk reduction is not included for system simplicity and compactness. Second, corrective optical components, such as the ones mentioned in [10,24], are not used for the same reason. The performance improvement and system complexity trade-off are subject to further investigation. Third, computational methods including deconvolution [58], Interferometric synthetic aperture microscopy [59], and digital refocusing [60] can be employed post-processing for lateral resolution optimization. Lastly, the off-axis performance of line illumination can be improved by using a Powell Lens. However, the alignment of the Powell lens [61] necessitates the need for high-precision mechanics that increase system cost and complexity. The overall dimension of our LF-OCT device is 20 × 15 × 20 cm^3 and connectable via a single USB 3.1 cable. The compact form factor overcomes the restrictions of implementing free space OCT systems and can be particularly advantageous for in-line quality inspection on production lines.

We highlighted three practical scenarios of the developed system in electronics, pharmaceuticals, and agricultural industries. The visualization and segmentation methods we proposed can accurately represent and measure the sub-surface structures of the samples. The 8-bit depth and reduced lateral resolution present challenges *in-vivo* imaging of biological samples. The in-vivo imaging capabilities of the system will be investigated with permission from our University Ethics Committee in the future.

Declaration of generative AI

During the preparation of this work, the authors used ChatGPT 3.0 in order to proofread certain sentences to improve readability. After using this tool, the authors reviewed and edited the content as needed and take full responsibility for the content of the publication.

Funding acknowledgments

This work is partially supported by the Engineering and Physical Sciences Research Council (EPSRC, Project references: EP/X01441X/1, EP/W006405/1, EP/W006308/2, and EP/W006642/1), and the Wellcome Trust (UK) (219574/Z/19/Z) and MRC CiC (MC_PC_19044). HL acknowledges the support from EP/L019922/1, the Royal Academy of Engineering Industrial Fellowships programme and BASF for providing the materials used in this study.

CRediT authorship contribution statement

Xingyu Yang: Writing – original draft, Visualization, Validation, Software, Methodology, Investigation, Formal analysis. **Zijian Zhang:** Writing – review & editing, Methodology. **Xinhua Li:** Writing – review & editing, Resources. **Hungyen Lin:** Writing – review & editing, Resources. **Samuel Lawman:** Writing – review & editing, Methodology. **Stoyan Stoyanov:** Writing – review & editing, Project administration. **Timothy Tilford:** Writing – review & editing, Project administration. **Yihua Hu:** Writing – review & editing, Project administration. **Yaochun Shen:** Supervision, Project administration, Investigation, Funding acquisition, Conceptualization. **Yalin Zheng:** Supervision, Project administration, Investigation, Funding acquisition, Conceptualization.

Declaration of competing interest

The authors declare the following financial interests/personal relationships which may be considered as potential competing interests:

Yalin Zheng reports financial support was provided by Wellcome Trust. Yaochun Shen reports financial support was provided by Engineering and Physical Sciences Research Council. If there are other authors, they declare that they have no known competing financial interests or personal relationships that could have appeared to influence the work reported in this paper.

Data availability

Data will be made available on request.

Supplementary materials

Supplementary material associated with this article can be found, in the online version, at doi:10.1016/j.optlaseng.2024.108631.

References

[1] Huang D, et al. Optical coherence tomography. Science 1991;254(5035):1178–81. https://doi.org/10.1126/science.1957169.
[2] Drexler W, Liu M, Kumar A, Kamali T, Unterhuber A, Leitgeb RA. Optical coherence tomography today: speed, contrast, and multimodality. J Biomed Opt 2014;19(7). 071412-071412.
[3] Drexler W, Fujimoto JG. Optical coherence tomography: technology and applications. Springer Science & Business Media; 2008.
[4] Fujimoto JG, Pitris C, Boppart SA, Brezinski ME. Optical coherence tomography: an emerging technology for biomedical imaging and optical biopsy. Neoplasia 2000;2 (1–2):9–25. https://doi.org/10.1038/sj.neo.7900071.
[5] Fercher AF, Hitzenberger CK, Kamp G, El-Zaiat SY. Measurement of intraocular distances by backscattering spectral interferometry. Opt Commun 1995;117(1–2): 43–8.
[6] Chinn S, Swanson E, Fujimoto J. Optical coherence tomography using a frequency-tunable optical source. Opt Lett 1997;22(5):340–2.
[7] Geitzenauer W, Hitzenberger CK, Schmidt-Erfurth UM. Retinal optical coherence tomography: past, present and future perspectives. Br J Ophthalmol 2011;95(2). https://doi.org/10.1136/bjo.2010.182170. -02-01.
[8] Leitgeb R, Hitzenberger C, Fercher AF. Performance of fourier domain vs. time domain optical coherence tomography. Opt Express 2003;11(8):889–94.
[9] Song G, Jelly ET, Chu KK, Kendall WY, Wax A. A review of low-cost and portable optical coherence tomography. Prog Biomed Eng 2021;3(3):032002. https://doi.org/10.1088/2516-1091/abfeb7.
[10] Kim S, Crose M, Eldridge WJ, Cox B, Brown WJ, Wax A. Design and implementation of a low-cost, portable OCT system. Biomed Opt Express 2018;9 (3):1232. https://doi.org/10.1364/boe.9.001232.
[11] McNamara PM, et al. Development of a first-generation miniature multiple reference optical coherence tomography imaging device. J Biomed Opt 2016;21 (12):126020. https://doi.org/10.1117/1.jbo.21.12.126020.
[12] Lu CD, et al. Handheld ultrahigh speed swept source optical coherence tomography instrument using a MEMS scanning mirror. Biomed Opt Express 2014;5(1):293. https://doi.org/10.1364/boe.5.000293.
[13] Venkateswaran N, Galor A, Wang J, Karp CL. Optical coherence tomography for ocular surface and corneal diseases: a review (in eng) Eye Vis (Lond) 2018;5:13. https://doi.org/10.1186/s40662-018-0107-0.
[14] Zuluaga AF, Richards-Kortum R. Spatially resolved spectral interferometry for determination of subsurface structure. Opt Lett 1999;24(8):519. https://doi.org/10.1364/ol.24.000519.
[15] Lawman S, et al. High resolution corneal and single pulse imaging with line field spectral domain optical coherence tomography. Opt Express 2016;24(11):12395. https://doi.org/10.1364/oe.24.012395.
[16] Zhang Z, et al. Rapid imaging and product screening with low-cost line-field Fourier domain optical coherence tomography. Sci Rep 2023;13(1):10809 [Online] Available: https://www.nature.com/articles/s41598-023-37646-4.
[17] Lawman S, Mason S, Kaye SB, Shen YC, Zheng Y. Accurate *in vivo* bowman's thickness measurement using mirau ultrahigh axial resolution line field optical coherence tomography. Transl Vis Sci Technol 2022;11(8):6. https://doi.org/10.1167/tvst.11.8.6.
[18] Fechtig DJ, et al. Line-field parallel swept source MHz OCT for structural and functional retinal imaging. Biomed Opt Express 2015;6(3):716. https://doi.org/10.1364/boe.6.000716.
[19] K. Neuhaus et al., "Real-time line-field OCT using low-cost high-speed camera," 10.1117/12.2652656, vol. 12367, 2023, 10.1117/12.2652656.
[20] Malone JD, Hussain I, Bowden AK. SmartOCT: smartphone-integrated optical coherence tomography. Biomed Opt Express 2023;14(7):3138. https://doi.org/10.1364/boe.492439.
[21] M.J.M. Marques, M. Fauchart, A. Bradu, and A.G.H. Podoleanu, "Evaluation of a commercial-grade camera for line field spectral-domain optical coherence tomography," 2019, SPIE, 10.1117/12.2511401. [Online]. Available: 10.1117/12.2511401.
[22] Wang L, Fu R, Xu C, Xu M. Methods and applications of full-field optical coherence tomography: a review. J Biomed Opt 2022;27(5). 050901-050901.
[23] Zhang Z, et al. Sub-surface imaging of soiled cotton fabric using full-field optical coherence tomography. Opt Express 2019;27(10):13951–64 [Online]. Available: https://opg.optica.org/oe/fulltext.cfm?uri=oe-27-10-13951&id=411879.

[24] Chen Z, Zhao C, Shen Y, Li P, Wang X, Ding Z. Ultrawide-field parallel spectral domain optical coherence tomography for nondestructive inspection of glass. Opt Commun 2015;341:122–30. https://doi.org/10.1016/j.optcom.2014.12.016.

[25] Shirazi M, et al. Fast industrial inspection of optical thin film using optical coherence tomography. Sensors 2016;16(10):1598. https://doi.org/10.3390/s16101598. 2016-09-28.

[26] Dong Y, Lawman S, Zheng Y, Williams D, Zhang J, Shen YC. Nondestructive analysis of automotive paints with spectral domain optical coherence tomography. Appl Opt 2016;55(13):3695–700. https://doi.org/10.1364/AO.55.003695. 2016/05/01.

[27] Lee SY, Lee C, Kim J, Jung HY. Application of optical coherence tomography to detect Cucumber green mottle mosaic virus (CGMMV) infected cucumber seed. Hortic Environ Biotechnol 2012;53(5):428–33. https://doi.org/10.1007/s13580-012-0071-x.

[28] Markl D, Hannesschläger G, Sacher S, Leitner M, Khinast JG. Optical coherence tomography as a novel tool for in-line monitoring of a pharmaceutical film-coating process. Eur J Pharm Sci 2014;55:58–67. https://doi.org/10.1016/j.ejps.2014.01.011.

[29] Wijesinghe RE, Lee SY, Kim P, Jung HY, Jeon M, Kim J. Optical sensing method to analyze germination rate of *Capsicum annum*seeds treated with growth-promoting chemical compounds using optical coherence tomography. J Biomed Opt 2017;22(9):091502. https://doi.org/10.1117/1.jbo.22.9.091502.

[30] X. Wang, Q. Wu, J. Zhu, J. Dai, and J. Mo, "Detect curing extent of conformal coating using speckle variance optical coherence tomography," 2019: SPIE, 10.1117/12.2537491. [Online]. Available: 10.1117/12.2537491.

[31] Tomlins PH, Wang RK. Theory, developments and applications of optical coherence tomography. J Phys D Appl Phys 2005;38(15):2519–35. https://doi.org/10.1088/0022-3727/38/15/002.

[32] Goldberg BD, et al. Performance of reduced bit-depth acquisition for optical frequency domain imaging. Opt Express 2009;17(19):16957. https://doi.org/10.1364/oe.17.016957.

[33] De Carlo TE, Romano A, Waheed NK, Duker JS. A review of optical coherence tomography angiography (OCTA). Int J Retina Vitr 2015;1(1). https://doi.org/10.1186/s40942-015-0005-8.

[34] Yasuno Y, et al. One-shot-phase-shifting Fourier domain optical coherence tomography by reference wavefront tilting. Opt Express 2004;12(25):6184. https://doi.org/10.1364/opex.12.006184.

[35] Huber R, Adler DC, Fujimoto JG. Buffered Fourier domain mode locking: unidirectional swept laser sources for optical coherence tomography imaging at 370,000 lines/s. Opt Lett 2006;31(20):2975. https://doi.org/10.1364/ol.31.002975.

[36] Lu Z, Kasaragod DK, Matcher SJ. Performance comparison between 8- and 14-bit-depth imaging in polarization-sensitive swept-source optical coherence tomography. Biomed Opt Express 2011;2(4):794. https://doi.org/10.1364/boe.2.000794.

[37] Hao Q, et al. High signal-to-noise ratio reconstruction of low bit-depth optical coherence tomography using deep learning. J Biomed Opt 2020;25(12). https://doi.org/10.1117/1.jbo.25.12.123702.

[38] Zhang Y, Li X, Wei L, Wang K, Ding Z, Shi G. Time-domain interpolation for Fourier-domain optical coherence tomography. Opt Lett 2009;34(12):1849. https://doi.org/10.1364/ol.34.001849.

[39] Leitgeb RA, et al. Ultrahigh resolution Fourier domain optical coherence tomography. Opt Express 2004;12(10):2156. https://doi.org/10.1364/opex.12.002156.

[40] Nakamura Y, Makita S, Yamanari M, Itoh M, Yatagai T, Yasuno Y. High-speed three-dimensional human retinal imaging by line-field spectral domain optical coherence tomography. Opt Express 2007;15(12):7103. https://doi.org/10.1364/oe.15.007103.

[41] Leitgeb R, Hitzenberger C, Fercher A. Performance of fourier domain vs time domain optical coherence tomography. Opt Express 2003;11(8):889. https://doi.org/10.1364/oe.11.000889.

[42] Ab R. The effect of temperature on the performance of uncooled semiconductor laser diode in optical network. J Comput Sci 2012;8(1):84–8. https://doi.org/10.3844/jcssp.2012.84.88.

[43] Agrawal A, Pfefer TJ, Woolliams PD, Tomlins PH, Nehmetallah G. Methods to assess sensitivity of optical coherence tomography systems. Biomed Opt Express 2017;8(2). https://doi.org/10.1364/BOE.8.000902. /02/02.

[44] Baroni M, Fortunato P, La Torre A. Towards quantitative analysis of retinal features in optical coherence tomography. Med Eng Phys 2007;29(4):432–41. https://doi.org/10.1016/j.medengphy.2006.06.003. 2007/05/01/.

[45] Ishikawa H, Stein DM, Wollstein G, Beaton S, Fujimoto JG, Schuman JS. Macular segmentation with optical coherence tomography. Invest. Ophthalmol. Vis. Sci. 2005;46(6):2012–7.

[46] Buades A, Coll B, Morel JM. A non-local algorithm for image denoising. In: Proceedings of the 2005 IEEE computer society conference on computer vision and pattern recognition (CVPR'05). 2. Ieee; 2005. p. 60–5.

[47] Zhan S, Azarian MH, Pecht MG. Surface insulation resistance of conformally coated printed circuit boards processed with no-clean flux. IEEE Trans Electron Packag Manuf 2006;29(3):217–23. https://doi.org/10.1109/tepm.2006.882496.

[48] Petrilli C. The basics of coating thickness measurement. Metal Finishing 2001;99(8):8–13. https://doi.org/10.1016/s0026-0576(01)81189-2.

[49] Shao X, et al. Nondestructive measurement of conformal coating thickness on printed circuit board with ultra-high resolution optical coherence tomography | IEEE Journals & Magazine | IEEE Xplore. IEEE Access 2019;7. https://doi.org/10.1109/ACCESS.2019.2896622.

[50] Shao X, Yu X, Chen X, Mo J, Liu L, Chen Z. Spectral-domain optical coherence tomography for conformal coating thickness measurement on printed circuit board. SPIE; 2018. https://doi.org/10.1117/12.2502193. 10.1117/12.2502193. [Online]. Available:.

[51] Zhang Z, Williams B, Zheng Y, Lin H, Shen Y. Differentiating generic versus branded pharmaceutical tablets using ultra-high-resolution optical coherence tomography. Coatings 2019;9(5):326. https://doi.org/10.3390/coatings9050326.

[52] Dong Y, Lin H, Abolghasemi V, Gan L, Zeitler JA, Shen YC. Investigating Intra-Tablet Coating Uniformity With Spectral-Domain Optical Coherence Tomography. J Pharm Sci 2017;106(2):546–53. https://doi.org/10.1016/j.xphs.2016.09.021.

[53] Lin H, et al. Measurement of the intertablet coating uniformity of a pharmaceutical pan coating process with combined terahertz and optical coherence tomography in-line sensing. J Pharm Sci 2017;106(4):1075–84. https://doi.org/10.1016/j.xphs.2016.12.012. 2017/04/01/.

[54] Lin H, Zhang Z, Markl D, Zeitler J, Shen Y. A review of the applications of OCT for analysing pharmaceutical film coatings. Appl. Sci. 2018;8(12):2700. https://doi.org/10.3390/app8122700.

[55] Bewley JD, Bradford KJ, Hilhorst HWM, Nonogaki H. Germination. New York: Springer; 2013. p. 133–81.

[56] Li D, Rajagopalan UM, De Silva YSK, Liu F, Kadono H. Biospeckle optical coherence tomography (bOCT) in the speedy assessment of the responses of the seeds of raphanus sativus L. (Kaiware Daikon) to acid mine drainage (AMD). Appl. Sci. 2021;12(1):355. https://doi.org/10.3390/app12010355.

[57] Li X, et al. Nondestructive in situ monitoring of pea seeds germination using optical coherence tomography. Plant Direct 2022;6(7):e428 [Online]. Available: https://www.ncbi.nlm.nih.gov/pmc/articles/PMC9277031/.

[58] T.S. Ralston, D.L. Marks, F. Kamalabadi, and S.A. Boppart, "Deconvolution methods for mitigation of transverse blurring in optical coherence tomography | IEEE Journals & Magazine | IEEE Xplore," 2024 doi:10.1109/TIP.2005.852469.

[59] Ahmad A, et al. Real-time in vivo computed optical interferometric tomography. Nat Photonics 2013;7(6). https://doi.org/10.1038/nphoton.2013.71. *2013 7:6*-04-21.

[60] Kumar A, Drexler W, Leitgeb RA. Numerical focusing methods for full field OCT: a comparison based on a common signal model. Opt Express 2014;22(13):16061–78. https://doi.org/10.1364/OE.22.016061. 2014/06/30.

[61] Chen K, Song W, Han L, Bizheva K. Powell lens-based line-field spectral domain optical coherence tomography system for cellular resolution imaging of biological tissue. Biomed Opt Express 2023;14(5):2003. https://doi.org/10.1364/boe.486980.